npj Computational Materials

www.nature.com/npjcompumats

ARTICLE OPEN

Check for updates

Tunable dynamical magnetoelectric effect in antiferromagnetic topological insulator $MnBi_2Te_4$ films

Tongshuai Zhu[1,4], Huaiqiang Wang[1,2,4], Haijun Zhang[1,3]✉ and Dingyu Xing[1,3]

Axion was postulated as an elementary particle to solve the strong charge conjugation and parity puzzle, and later axion was also considered to be a possible component of dark matter in the universe. However, the existence of axions in nature has not been confirmed. Interestingly, axions arise out of pseudoscalar fields derived from the Chern–Simons theory in condensed matter physics. In antiferromagnetic insulators, the axion field can become dynamical due to spin-wave excitations and exhibits rich exotic phenomena, such as axion polariton. However, antiferromagnetic dynamical axion insulator has yet been experimentally identified in realistic materials. Very recently, $MnBi_2Te_4$ was discovered to be an antiferromagnetic topological insulator with a quantized static axion field protected by inversion symmetry $\mathcal{P}$ and magnetic-crystalline symmetry $\mathcal{S}$. Here, we studied $MnBi_2Te_4$ films in which both the $\mathcal{P}$ and $\mathcal{S}$ symmetries are spontaneously broken and found that substantially enhanced dynamical magnetoelectric effects could be realized through tuning the thickness of $MnBi_2Te_4$ films, temperature, or element substitutions. Our results show that thin films of $MnBi_2Te_4$ and related compounds could provide a promising material platform to experimentally study axion electrodynamics.

npj Computational Materials (2021)7:121 ; https://doi.org/10.1038/s41524-021-00589-3

INTRODUCTION

In condensed matter physics, an effective axion field can be derived from the (4+1)-dimensional Chern-Simons theory of topological insulators (TIs)[1,2], described by an axion action $S_\theta = \frac{\theta}{2\pi}\frac{e^2}{h}\int d^3x dt \mathbf{E}\cdot\mathbf{B}$, in which $\mathbf{E}$ and $\mathbf{B}$ are the electromagnetic fields inside the insulators, e is the charge of an electron, h is Planck's constant, θ is the dimensionless pseudoscalar parameter as the axion field[3]. The axion field θ is odd under the time reversal symmetry $\mathcal{T}$ or spatial inversion symmetry $\mathcal{P}$, so it is quantized to π (mod 2π) for TIs and 0 (mod 2π) for normal insulators (NIs) if $\mathcal{T}$ or $\mathcal{P}$ is preserved. Such a quantized θ can lead to the image magnetic monopole effect[4], the quantized magneto-optical Faraday/Kerr effect[5–12], the topological magnetoelectric effect (TME)[2,13–18] and the half-integer quantum Hall effect on the $\mathcal{T}$-breaking surface of TIs[2]. Recently, the axion field in condensed matters was studied in magnetic topological insulators[19–27], topological-material heterostructures[28,29], and charge-density-wave Weyl semimetals[30,31]. An overall review of the axion physics in condensed matters can be found in refs. [32,33].

In antiferromagnetic (AFM) insulators, the axion field θ can be an unquantized value, once both $\mathcal{T}$ and $\mathcal{P}$ are broken. The spin-wave excitations can induce fluctuations of the axion field[34–36], called as the dynamical axion field (DAF) $\theta(\mathbf{r}, t)$ which has spatial and temporal dependence. $\theta(\mathbf{r}, t)$ can lead to rich dynamical magnetoelectric (ME) effects, for example, the dynamical chiral magnetic effect[37–40], anomalous Hall effect[37], axionic polariton[34,41] and unconventional electromagnetic effects[42–44]. In principle, generic AFM insulators may exhibit the DAFs, such as Cr_2O_3[15,45,46], but the DAFs turn out to be too weak to be detected[36]. Large DAF requires the topologically nontrivial AFM insulators described by nonzero spin Chern numbers[47]. Recently, layered material $Mn_2Bi_2Te_5$ and the superlattice $(MnBi_2Te_4)_2(Bi_2Te_3)$ were predicted to host large DAFs[36,47], denoted as DAF insulators. However, the experimental synthesis of them has not been reported. Therefore, the challenge is to discover realistic DAF insulators.

Recently, bulk $MnBi_2Te_4$ was discovered to be an AFM TI and it hosts a quantized axion field $\theta = \pi$ protected by the inversion symmetry $\mathcal{P}$ and the magnetic-crystalline symmetry $\mathcal{S} = \mathcal{T}\tau_{1/2}$, where $\tau_{1/2}$ is the half-translation operator[22,23,25,48–62]. Interestingly, both $\mathcal{P}$ and $\mathcal{S}$ are spontaneously broken in $MnBi_2Te_4$ films with even septuple layers (SLs). In this article, our results indicate that the fluctuations of AFM order can lead to substantially enhanced dynamical ME effects in $MnBi_2Te_4$ thin films, induced by the $\mathcal{P}$ and $\mathcal{S}$ breaking.

As shown in Fig. 1a, the AFM TI $MnBi_2Te_4$[22] consists of SLs coupled to each other by a Van der Waals-type interaction. It features an A-type AFM magnetic ground state with the out-of-plane easy axis. Although the magnetic order explicitly breaks the $\mathcal{T}$, the bulk $MnBi_2Te_4$ possesses the $\mathcal{S}$, marked in Fig. 1a. In addition, the $\mathcal{P}$ is preserved for the bulk $MnBi_2Te_4$ with the inversion center at the Mn layer in the middle of each SL. Interestingly, both the $\mathcal{S}$ and $\mathcal{P}$ are explicitly broken in even-SL $MnBi_2Te_4$ thin films due to the finite size, schematically shown in Fig. 1b. As a result, the restriction for the quantization of the axion field θ is removed, which will lead to a tunable dynamical ME effect.

RESULTS

Effective model analysis

We start from the low-energy effective Hamiltonian of bulk $MnBi_2Te_4$. Taking the relevant symmetries $\mathcal{S}$, $\mathcal{P}$ and $\mathcal{C}_{3z}$ into account, the four-band $\mathbf{k}\cdot\mathbf{p}$ model up to the third order of $\mathbf{k}$ can

[1]National Laboratory of Solid State Microstructures, School of Physics, Nanjing University, Nanjing, China. [2]Department of Physics, University of Zurich, Zurich, Switzerland. [3]Collaborative Innovation Center of Advanced Microstructures, Nanjing University, Nanjing, China. [4]These authors contributed equally: Tongshuai Zhu, Huaiqiang Wang. ✉email: zhanghj@nju.edu.cn

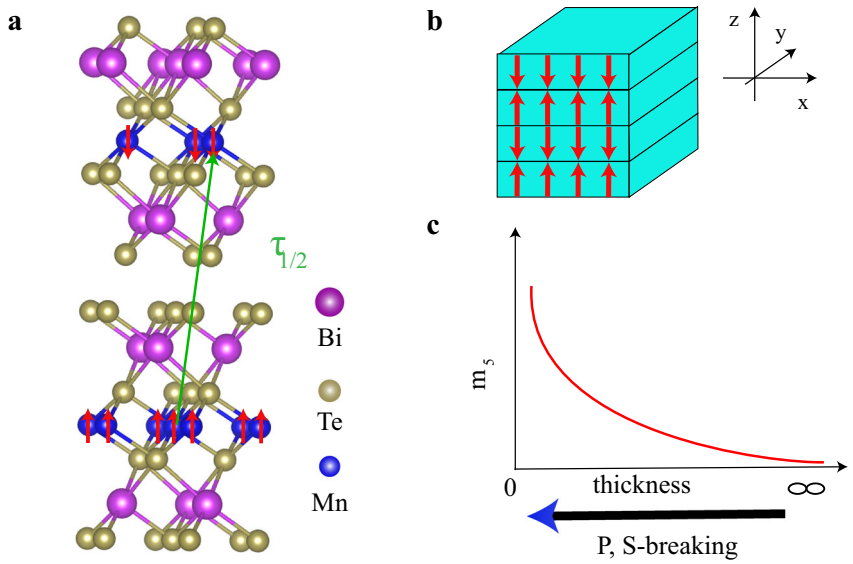

Fig. 1 Schematic of $\mathcal{P}$, $\mathcal{S}$-breaking mass in $MnBi_2Te_4$ thin films. a Crystal structure of $MnBi_2Te_4$. The red arrows denote the spin moment of Mn atoms and the green arrows represent the half-translation operator $\tau_{1/2}$ for the $\mathcal{S}$ symmetry. **b** Schematic of $MnBi_2Te_4$ thin films with even septuple layers grown along the easy axis (the *z*-direction). **c** Schematic of the $\mathcal{P}$, $\mathcal{S}$-breaking mass m_5 in $MnBi_2Te_4$ thin films. m_5 expects to increase when the film thickness decreases due to the $\mathcal{P}$, $\mathcal{S}$-breaking.

be obtained as[22] $H = H_0 + H_3$, where

$$H_0 = \epsilon(\mathbf{k})\Gamma_0 + \sum_{i=1}^{5} d_i(\mathbf{k})\Gamma^i, \tag{1}$$

with $d_i(\mathbf{k}) = (A_2k_y, -A_2k_x, A_1k_z, M(\mathbf{k}), 0)$, $\epsilon(\mathbf{k}) = C_0 + D_1k_z^2 + D_2(k_x^2 + k_y^2)$, and $M(\mathbf{k}) = m_4 + B_1k_z^2 + B_2(k_x^2 + k_y^2)$. Here, m_4 is the mass term with $m_4 < 0$ ($m_4 > 0$) depicting the inverted (normal) band structure. The Dirac matrices are given by $\Gamma_{0,1,\ldots,5} = (\tau_0 \otimes \sigma_0, \tau_x \otimes \sigma_x, \tau_x \otimes \sigma_y, \tau_y \otimes \sigma_0, \tau_z \otimes \sigma_0, \tau_x \otimes \sigma_z)$, where $\tau_{x,y,z}$ and $\sigma_{x,y,z}$ denote the Pauli matrices for the orbital and spin, respectively. The third order term H_3 is given explicitly by

$$H_3 = R_1\left(k_x^3 - 3k_xk_y^2\right)\Gamma_5 + R_2\left(3k_x^2k_y - k_y^3\right)\Gamma_3. \tag{2}$$

The detailed parameters can be obtained by fitting with first-principles band structure and have already been provided in ref. [22].

For $MnBi_2Te_4$ thin films, both $\mathcal{S}$ and $\mathcal{P}$ are broken, but the combined symmetry $\mathcal{PT}$ is preserved. Based on the symmetry analysis, a mass term $m_5\Gamma_5$ to the leading order adds to the effective Hamiltonian of $MnBi_2Te_4$ thin films and significantly changes the axion field θ from the quantized value (π). Actually, the mass term $m_5\Gamma_5$ indicates an effective staggered Zeeman field generated by the AFM order[34]. Due to the finite-size effect, it expects to decrease with increasing thickness of the films, and finally vanishes for the bulk limit, as illustrated in Fig. 1c. This is in contrast to the three-dimensional (3D) DAF insulator[34,36,47] with a non-vanishing m_5 in the bulk limit. Based on the effective Hamiltonian, the energy gap at the Γ point of $MnBi_2Te_4$ thin films is found to be $E_{gap} = 2\sqrt{m_4^2 + m_5^2}$. When the strength of spin-orbit coupling (SOC) λ is tuned from zero to the realistic value λ_0, the band inversion is induced along with the mass term m_4 changing from $m_4 > 0$ to $m_4 < 0$, and the energy gap reaches the minimum $E_{gap} = 2|m_5|$ when the band inversion happens ($m_4 = 0$). Based on this picture, we can quantitatively characterize the mass m_5 for $MnBi_2Te_4$ thin films.

As an example, the first-principles band structures of 12-SL $MnBi_2Te_4$ with different SOC are calculated, shown in Fig. 2a. The SOC dependence of E_{gap} is further extracted and shown in Fig. 2b. When SOC is weak, the band structures indicate an energy gap E_{gap} without a band inversion. As expected, when increasing SOC, E_{gap} decreases to a minimum around SOC ($\lambda \sim 0.9\lambda_0$) without gap closing, and then increases with a band inversion. In Fig. 2c, it explicitly shows the mass m_5 as a function of the thickness of *N* bi-SL $MnBi_2Te_4$ thin films (red line), which indeed gradually decreases with increasing *N*. For comparison, we also present the result of m_5 for $Mn_2Bi_2Te_5$ thin films (blue line). It is obvious that for large *N* towards the bulk limit, m_5 approaches zero (a finite value) for $MnBi_2Te_4$ ($Mn_2Bi_2Te_5$), as expected. Note that m_5 of $MnBi_2Te_4$ films is tunable to zero within a larger range than that of $Mn_2Bi_2Te_5$ films, as shown in Fig. 2c. Furthermore, it is numerically found that m_5 exhibits an approximately linear behavior against 1/*N*, namely, the inverse of the thickness for both $MnBi_2Te_4$ and $Mn_2Bi_2Te_5$ films, as shown in Fig. 2d.

Dynamical magnetoelectric effect

The application of an electric field can induce a magnetization, and reversely, the application of a magnetic field can lead to a polarization, which is the typical ME effect. In 3D TIs, such as Bi_2Se_3[63], the ME response is isotropic, which can be described by the effective axion action S_θ with the quantized axion field $\theta = \pi$, protected by the time reversal symmetry $\mathcal{T}$. In AFM TI $MnBi_2Te_4$, both $\mathcal{P}$ and $\mathcal{S}$ constrain the axion field θ to the quantized value of π. However, for even-SL $MnBi_2Te_4$ thin films, all $\mathcal{P}$, $\mathcal{T}$ and $\mathcal{S}$ symmetries are broken and the mass m_5 is induced, thus rendering an unquantized θ. It should be pointed out that due to the finite-size effect in $MnBi_2Te_4$ thin films, the ME response is generically anisotropic[64]. Moreover, since m_5 is related to the inherently fluctuating AFM order, the axion field will be time dependent $\partial_t\theta(t) \neq 0$, leading to the dynamical ME effect. In the following, we will show that the dynamical ME effect can be realized and substantially tuned by adjusting the film thickness, temperature or element substitutions.

Here, we consider applying a magnetic field **B** in the plane of $MnBi_2Te_4$ thin films (e.g. the *x*-axis in Fig. 1a), which will induce a charge polarization **P** in the same direction. To describe such a ME response, we need to calculate the ME coefficient α defined as $\mathbf{P} = -\alpha\mathbf{B}$ and it can be obtained from the quantity $\gamma \equiv (1/d)\int_{-d/2}^{d/2} dz\eta(z)$ through $\alpha = \gamma(e^2/2h)$[17,64]. Here, $\eta(z)$ is a

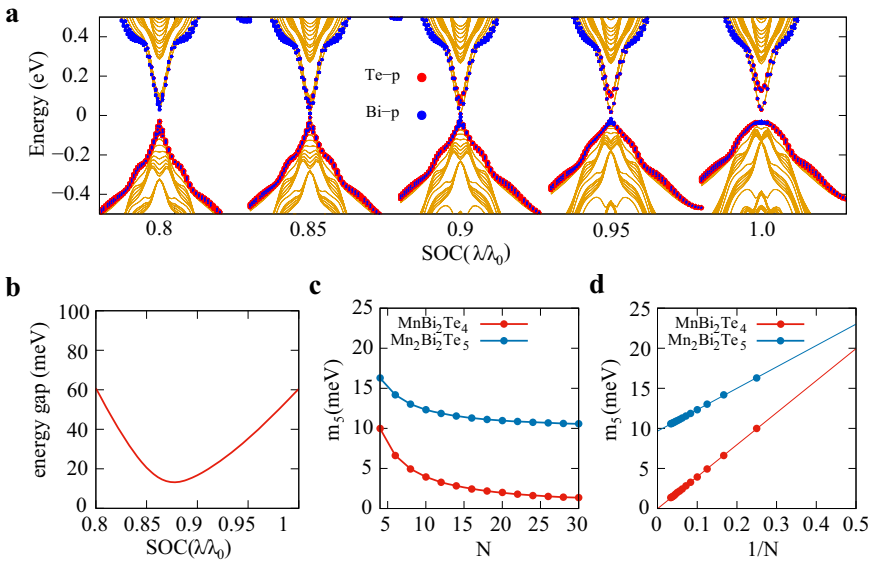

Fig. 2 Finite-size effect of $MnBi_2Te_4$ thin films. a The evolution of the band structure of the 12-SL $MnBi_2Te_4$ thin film as a function of the strength of the SOC λ/λ_0. **b** The evolution of the energy gap with the SOC strength. The energy gap first goes smaller and then goes larger without exactly closing. It is clear to see a minimum energy gap when increasing the SOC, which corresponds to $2|m_5|$ (the $\mathcal{P}$, $\mathcal{S}$-breaking mass). **c,d** The mass m_5 versus the thickness of $MnBi_2Te_4$ (red) and $Mn_2Bi_2Te_5$ (blue) thin films. N presents the number of bi-SLs of $MnBi_2Te_4$ films or (nonuple layers)NLs of $Mn_2Bi_2Te_5$ films.

dimensionless function defined as

$$\eta(z) = 2\int_{-d/2}^{d/2} \mathrm{d}z' z' \Pi_{xy}(z,z'), \tag{3}$$

where the current correlation function $\Pi_{xy}(z,z')$ is given by the Kubo formula,

$$\Pi_{xy}(z,z') = \frac{\hbar^2}{2\pi e}\int d^2\mathbf{k} \sum_{n\neq m} f(\epsilon_{n\mathbf{k}}) \times 2\mathrm{Im}\left[\frac{\langle n\mathbf{k}|j_x(\mathbf{k},z)|m\mathbf{k}\rangle\langle m\mathbf{k}|j_y(\mathbf{k},z')|n\mathbf{k}\rangle}{(\epsilon_{n\mathbf{k}}-\epsilon_{m\mathbf{k}})^2}\right]. \tag{4}$$

Here, $|n\mathbf{k}\rangle$ is the normalized Bloch wavefunction of the n-th electron subband, and $j(\mathbf{k},z) = (e/\hbar)\partial_{\mathbf{k}}H(\mathbf{k},z)$ represents the x-y plane current density operator, where $H(\mathbf{k},z)$ is obtained by discretizing the system into a tight-binding model along the z-direction and fixing the periodic boundary condition in the x-y plane to preserve k_x and k_y as good quantum numbers.

In the bulk limit, the quantity γ is related to the axion field by $\gamma = \theta/\pi$. Considering the inherent AFM fluctuations with δm_5, θ can be divided into a static part θ_0 and a dynamical part $\delta\theta(t)$. Similarly, γ is also comprised of a static part γ_0 and a dynamical part $\delta\gamma(t)$ given by $\delta\gamma = \delta m_5/g$ with the coefficient $1/g = \partial\gamma/\partial m_5$ to the linear order of δm_5. We can see that $1/g$ is a key quantity for a large dynamical ME effect under AFM fluctuations δm_5.

In Fig. 3a, we present the quantity γ_0 as a function of the thickness of N bi-SLs $MnBi_2Te_4$ thin films (red line) and we take $Mn_2Bi_2Te_5$ films (yellow line) for comparison. It can be seen that with increasing N, γ_0 gradually increases and approaches 1 at the bulk limit with $N\to\infty$ for $MnBi_2Te_4$ while it approaches a finite value (<1) for $Mn_2Bi_2Te_5$ films at the bulk limit. The dependence of γ_0 on the mass term m_5 for $MnBi_2Te_4$ films with different thicknesses ($N = 4, 6, 8, 16$) are shown in Fig. 3b. When N is large, γ_0 quickly increases when m_5 is small. With increasing m_5, γ_0 exhibits a linear decrease for all films, which indicates a large m_5 tends to suppress γ_0. Based on the dependence of γ_0 on m_5, the dependence of the the quantity $1/g$ on m_5 can be further obtained, shown in Fig. 3d. The generic feature is that $1/g$ increases with decreasing m_5, and approaches the maximum value when $m_5\to 0$. It is notable that there is a broad range of m_5 to a large $1/g$ for thin films (e.g. $N = 4, 6, 8$), while that range of m_5 is extremely reduced for thick films (e.g. $N = 16$). We then investigate the tunability of $1/g$ from the film thickness, temperature and element substitutions.

We first inspect the finite-size effect. Based on first-principles calculations of m_5 presented in Fig. 2c, the dependence of $1/g$ on varying N is shown in Fig. 3c. We can see that $1/g$ is large for the ultrathin limit, and quickly decreases with increasing the film thickness (N), and then crosses zero from positive to negative, and gradually saturates. Secondly, we discuss the temperature effect. $\mathbf{M}^- = 1/2(\langle\mathbf{S}_{iA}\rangle - \langle\mathbf{S}_{iB}\rangle)$ is taken as the AFM order parameter, where i denotes the unit cell and A/B denotes the magnetic sites. The AFM order is in the $\hat{z}$ direction ($\mathbf{M}^- = M^-\hat{z}$) for $MnBi_2Te_4$ films and it leads to $m_5 \propto M_z^{-}$[34]. With increasing the temperature from zero to the Néel temperature, M_z^- inevitably decreases from the maximum value to zero. Consequently, for $MnBi_2Te_4$ thin films, the m_5 can be continuously tuned by the temperature, from the maximum value at zero temperature to zero near the Néel temperature T_N. Therefore, a tunable range of substantially enhanced $1/g$ is obtained through adjusting the temperature from zero to T_N (see the shaded regions). According to Fig. 3a, d, the ultrathin films (e.g. $N = 4$) have a broad tunable range of m_5 to large $1/g$, but a small static γ_0. The bulk limit films have a tiny range of m_5 to large $1/g$ (e.g. $N = 16$). Most interestingly, the proper thin films (e.g. $N = 6, 8$) have both a broad tunable range of m_5 to large $1/g$ and a large static γ_0, which should be a promising choice for experiments.

At last, we investigate the effect of element substitutions. The mass term m_4, with $m_4 < 0$ ($m_4 > 0$) indicates a topologically nontrivial (trivial) electronic structure. Interestingly, m_4 can be experimentally tuned through element substitutions in $Mn(Bi_{1-x}Sb_x)_2(Te_{1-y}Se_y)_4$ materials. Here, we choose three representative m_4, namely, two in the band-inverted nontrivial regime [$m_4 = -116.7$ meV (red lines) is taken from ref. [22] and $m_4 = -50$ meV (blue lines) presents a moderate band inversion], and one in the trivial regime [$m_4 = 50$ meV (yellow lines)], to show γ_0 and $1/g$ for different thick films in Fig. 3e, f. In the topologically trivial case, $\gamma_0 \sim 0$. In the topologically nontrivial case, it can be seen that a larger $|m_4|$ exhibits a larger γ_0, which approaches 1 for $N\to\infty$. According to Fig. 3f, $1/g$ in the topologically trivial case is obviously negligible

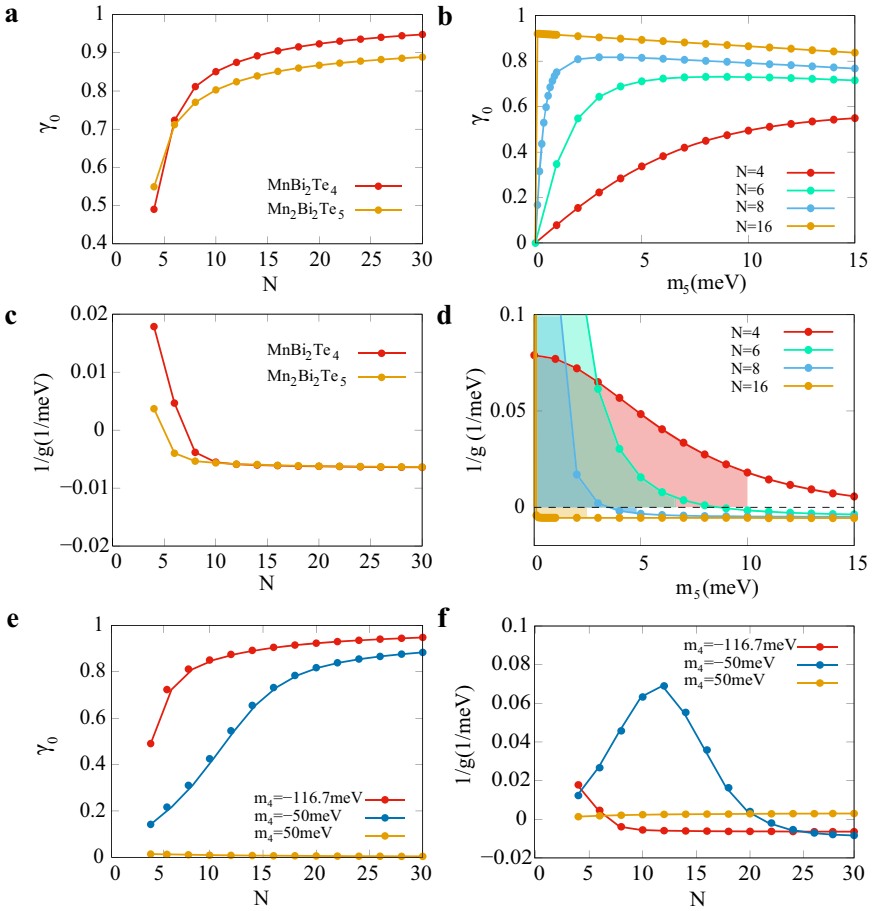

Fig. 3 Dynamical magnetoelectic effect. a, **c** The ME quantity γ_0 (**a**) and $1/g$ (**c**) versus the thickness with N bi-SLs for $MnBi_2Te_4$ (red) and NLs $Mn_2Bi_2Te_5$ (yellow) thin films, where values of m_5 are obtained from first-principles calculations. **b**, **d** γ_0 (**b**) and $1/g$ (**d**) as a function of m_5 for films with different thickness ($N = 4, 6, 8, 16$). The shaded regions in (**d**) denote the substantially tunable range $1/g$ of realistic $MnBi_2Te_4$ thin films by decreasing m_5 with increasing temperatures up to the Néel temperature. **e**, **f** γ_0 (**e**) and $1/g$ (**f**) as a function of the thickness (N bi-SLs) of films for three representative values of the mass term m_4, where negative (positive) m_4 represents topologically nontrivial (trivial) band structure with (without) the band inversion. The mass term m_4 can be tuned through the element substitution of $Mn(Bi_{1-x}Sb_x)_2(Te_{1-y}Se_y)_4$.

compared to that in the topologically nontrivial case. As for the nontrivial case, overall speaking, a weaker band inversion with smaller $|m_4|$ ($m_4 < 0$) leads to a larger magnitude of $1/g$, shown in Fig. 3f. Notably, the band-inversion magnitude could be modified by the finite-size effect[65], as reflected by the non-monotonic behavior (blue line) of $1/g$ on N in Fig. 3f.

Experimental detection

Many interesting experimental designs of axion electrodynamics have been proposed, including the instability in an external electric field[42], the recent proposal of unconventional level attraction in cavity axion polariton[41] and the proposal to detect dark matter axions[66], but the experimental progress is quite slow due to the lack of realistic DAF materials. The tunable dynamical ME effect in $MnBi_2Te_4$ thin films expects to be used for these proposals. Here, we quantitatively estimate that it is experimentally accessible to detect the dynamical ME effect in $MnBi_2Te_4$ thin films through the current transport techniques. The basic idea is to measure the in-plane response current induced by the chiral magnetic effect, given by $j_{CME} = -\frac{e^2}{2h}\frac{\partial\delta\gamma}{\partial t}B$, where B is the uniform inplane magnetic field. Since the dynamical ME coefficient $\delta\gamma$ is proportional to the change of the AFM order δm_5, a time-varying $\delta\gamma$ can be driven by AFM resonance[37], in the presence of both a uniform magnetic field along the out-of-plane (z) direction and a microwave magnetic field along the in-plane direction. Therefore,

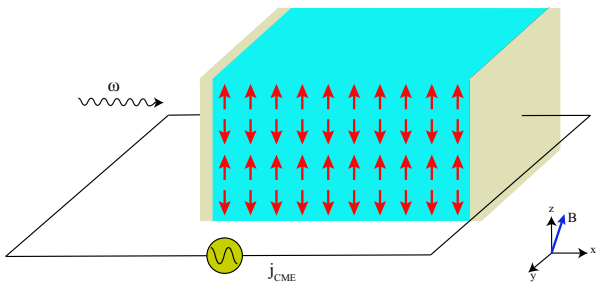

Fig. 4 Experimental setup for detecting the tunable dynamical ME effect. A tilted static magnetic is applied with components along both x and z directions. A microwave magnetic field with a frequency of ω is applied along the in-plane x-direction to drive the AFM resonance. The chiral magnetic effect due to the time-varying dynamical ME coefficient will lead to a measurable inplane response current.

as schematically illustrated in Fig. 4, we apply a tilted static magnetic field **B**, with components B_x and B_z along x and z directions, respectively, and a microwave magnetic field $\mathbf{B}_\omega$ with a frequency of ω along the inplane direction. Taking $\delta\gamma(t) \approx \delta m_5^0 \sin(\omega t)/g$, where δm_5^0 is the amplitude of the driven

AFM fluctuation, the response current can be obtained as

$$j_{\mathrm{CME}} = -\frac{e^2}{2h}\frac{\delta m_5^0 \omega B_x}{g}\cos(\omega t). \quad (5)$$

Note that since $1/g$ can be tuned by the film thickness, temperature, and element substitutions, the magnitude of j_{CME} can thus be tunable. As a concrete example, we choose $N = 6$ bi-SL $MnBi_2Te_4$ thin film with $\gamma_0 = 0.6$, $m_5 = 3$ meV, and $1/g = 0.1$ meV^{-1}. The other parameters are chosen typically as $B_x = 0.1$ T, $\omega/2\pi = 20$ GHz, and $\delta m_5^0 = 0.5$ meV. Finally, the amplitude of j_{CME} is approximated as $1.2Acm^{-2}$, which can be further much enhanced through tuning $1/g$ (see the shade region in Fig. 3d), therefore it is accessible by current transport experimental techniques.

DISCUSSION

To summarize, our work presents that AFM TI films $MnBi_2Te_4$ family, which have been successfully synthesized and well studied, provide a promising material platform to realize the dynamical ME effects. More interestingly, the dynamical ME effect is tunable and even substantially enhanced through engineering the thickness of films, temperature or element substitutions. It expects to be experimentally detectable and should be used to realize those exotic axion electrodynamics previously proposed.

METHODS

Computational details

We performed the first-principles calculations for bulk $MnBi_2Te_4$ and $Mn_2Bi_2Te_5$ with different SOC through employing the Vienna ab-initio simulation package(VASP)[67,68] and the generalized gradient approximation (GGA) with the Perdew–Burke–Ernzerhof(PBE)[69,70] type exchange-correlation potential was adopted, with the energy cutoff fixed to 420 eV. By considering the transition metal Mn, GGA+U functional with U = 3 eV for Mn d orbitals for all the results in this work. The k-point sampling grid of Brillouin zone in the self-consistent process was a Γ-centered Monkhorst–Pack k-point mesh of $8 \times 8 \times 4$ for the bulk systems, and a total energy tolerance 10^{-7}eV was adopted for self-consistent convergence. For $MnBi_2Te_4$ and $Mn_2Bi_2Te_5$ films, we employed the maximally localized Wanneir functions (MLWF) from the first-principles calculations[71,72] to construct tight-binding Hamiltonians for different thickness. The Mn − d, Te − p and Bi − p orbitals were initialized for MLWFs by Wannier90[73].

DATA AVAILABILITY

The data used in this study are available from the corresponding author upon reasonable request.

Received: 26 March 2021; Accepted: 6 July 2021;
Published online: 26 July 2021

REFERENCES

1. Qi, X.-L. & Zhang, S.-C. Topological insulators and superconductors. *Rev. Mod. Phys.* **83**, 1057 (2011).
2. Qi, X.-L., Hughes, T. L. & Zhang, S.-C. Topological field theory of time-reversal invariant insulators. *Phys. Rev. B* **78**, 195424 (2008).
3. Wilczek, F. Two applications of axion electrodynamics. *Phys. Rev. Lett.* **58**, 1799 (1987).
4. Qi, X.-L., Li, R., Zang, J. & Zhang, S.-C. Inducing a magnetic monopole with topological surface states. *Science* **323**, 1184 (2009).
5. Maciejko, J., Qi, X.-L., Drew, H. D. & Zhang, S.-C. Topological Quantization in Units of the Fine Structure Constant. *Phys. Rev. Lett.* **105**, 166803 (2010).
6. Tse, W.-K. & MacDonald, A. H. Giant magneto-optical kerr effect and universal faraday effect in thin-film topological insulators. *Phys. Rev. Lett.* **105**, 057401 (2010).
7. Ochiai, T. Theory of light scattering in axion electrodynamics. *J. Phys. Soc. Jpn* **81**, 094401 (2012).
8. Karch, A. Electric-magnetic duality and topological insulators. *Phys. Rev. Lett.* **103**, 171601 (2009).
9. Mal'shukov, A. G., Skarsvåg, H. & Brataas, A. Nonlinear magneto-optical and magnetoelectric phenomena in topological insulator heterostructures. *Phys. Rev. B* **88**, 245122 (2013).
10. Wu, L. et al. Quantized Faraday and Kerr rotation and axion electrodynamics of a 3D topological insulator. *Science* **354**, 1124 (2016).
11. Okada, K. N. et al. Terahertz spectroscopy on Faraday and Kerr rotations in a quantum anomalous Hall state. *Nat. Commun.* **7**, 12245 (2016).
12. Dziom, V. et al. Observation of the universal magnetoelectric effect in a 3D topological insulator. *Nat. Commun.* **8**, 15197 (2017).
13. Essin, A. M., Moore, J. E. & Vanderbilt, D. Magnetoelectric polarizability and axion electrodynamics in crystalline insulators. *Phys. Rev. Lett.* **102**, 146805 (2009).
14. Rosenberg, G. & Franz, M. Witten effect in a crystalline topological insulator. *Phys. Rev. B* **82**, 035105 (2010).
15. Coh, S., Vanderbilt, D., Malashevich, A. & Souza, I. Chern-Simons orbital magnetoelectric coupling in generic insulators. *Phys. Rev. B* **83**, 085108 (2011).
16. Morimoto, T., Furusaki, A. & Nagaosa, N. Topological magnetoelectric effects in thin films of topological insulators. *Phys. Rev. B* **92**, 085113 (2015).
17. Wang, J., Lian, B., Qi, X.-L. & Zhang, S.-C. Quantized topological magnetoelectric effect of the zero-plateau quantum anomalous Hall state. *Phys. Rev. B* **92**, 081107 (2015).
18. Zirnstein, H.-G. & Rosenow, B. Time-reversal-symmetric topological magnetoelectric effect in three-dimensional topological insulators. *Phys. Rev. B* **96**, 201112 (2017).
19. Mong, R. S. K., Essin, A. M. & Moore, J. E. Antiferromagnetic topological insulators. *Phys. Rev. B* **81**, 245209 (2010).
20. Wan, X., Vishwanath, A. & Savrasov, S. Y. Computational design of axion insulators based on 5d spinel compounds. *Phys. Rev. Lett.* **108**, 146601 (2012).
21. Turner, A. M., Zhang, Y., Mong, R. S. K. & Vishwanath, A. Quantized response and topology of magnetic insulators with inversion symmetry. *Phys. Rev. B* **85**, 165120 (2012).
22. Zhang, D. et al. Topological axion states in the magnetic insulator $MnBi_2$ Te_4 with the quantized magnetoelectric effect. *Phys. Rev. Lett.* **122**, 206401 (2019).
23. Gong, Y. et al. Experimental realization of an intrinsic magnetic topological insulator. *Chin. Phys. Lett.* **36**, 076801 (2019).
24. Xu, Y., Song, Z., Wang, Z., Weng, H. & Dai, X. Higher-order topology of the axion insulator $EuIn_2$ As_2. *Phys. Rev. Lett.* **122**, 256402 (2019).
25. Liu, C. et al. Robust axion insulator and Chern insulator phases in a two-dimensional antiferromagnetic topological insulator. *Nat. Mater.* **19**, 522 (2020).
26. Li, H. et al. Dirac surface states in intrinsic magnetic topological insulators $EuSn_2$ As_2 and $MnBi_{2n}$ Te_{3n+1}. *Phys. Rev. X* **9**, 041039 (2019).
27. Zhang, R.-X., Wu, F. & Das Sarma, S. Möbius insulator and higher-order topology in $MnBi_{2n}$ Te_{3n+1}. *Phys. Rev. Lett.* **124**, 136407 (2020).
28. Mogi, M. et al. A magnetic heterostructure of topological insulators as a candidate for an axion insulator. *Nat. Mater.* **16**, 516 (2017).
29. Xiao, D. et al. Realization of the axion insulator state in quantum anomalous hall sandwich heterostructures. *Phys. Rev. Lett.* **120**, 056801 (2018).
30. Wang, Z. & Zhang, S.-C. Chiral anomaly, charge density waves, and axion strings from Weyl semimetals. *Phys. Rev. B* **87**, 161107 (2013).
31. Gooth, J. et al. Axionic charge-density wave in the Weyl semimetal $(TaSe_4)_2$ I. *Nature* **575**, 315 (2019).
32. Nenno, D. M., Garcia, C. A. C., Gooth, J., Felser, C. & Narang, P. Axion physics in condensed-matter systems. *Nat. Rev. Phys.* **2**, 682 (2020).
33. Sekine, A. & Nomura, K. Axion electrodynamics in topological materials. *J. Appl. Phys.* **129**, 141101 (2021).
34. Li, R., Wang, J., Qi, X.-L. & Zhang, S.-C. Dynamical axion field in topological magnetic insulators. *Nat. Phys.* **6**, 284 (2010).
35. Wang, J., Li, R., Zhang, S.-C. & Qi, X.-L. Topological magnetic insulators with corundum structure. *Phys. Rev. Lett.* **106**, 126403 (2011).
36. Zhang, J. et al. Large dynamical axion field in topological antiferromagnetic insulator Mn_2 Bi_2 Te_5. *Chin. Phys. Lett.* **37**, 077304 (2020).
37. Sekine, A. & Nomura, K. Chiral magnetic effect and anomalous hall effect in antiferromagnetic insulators with spin-orbit coupling. *Phys. Rev. Lett.* **116**, 096401 (2016).
38. Sumiyoshi, H. & Fujimoto, S. Torsional chiral magnetic effect in a Weyl semimetal with a topological defect. *Phys. Rev. Lett.* **116**, 166601 (2016).
39. Li, Q. et al. Chiral magnetic effect in $ZrTe_5$. *Nat. Phys.* **12**, 550 (2016).
40. Sekine, A. & Chiba, T. Electric-field-induced spin resonance in antiferromagnetic insulators: inverse process of the dynamical chiral magnetic effect. *Phys. Rev. B* **93**, 220403 (2016).
41. Xiao, Y. et al. Unconventional level attraction in cavity axion polariton of antiferromagnetic topological insulator. Preprint at https://arxiv.org/abs/2011.04916 (2020).

42. Ooguri, H. & Oshikawa, M. Instability in magnetic materials with a dynamical axion field. *Phys. Rev. Lett.* **108**, 161803 (2012).
43. Taguchi, K. et al. Electromagnetic effects induced by a time-dependent axion field. *Phys. Rev. B* **97**, 214409 (2018).
44. Imaeda, T., Kawaguchi, Y., Tanaka, Y. & Sato, M. Axion instability and nonlinear electromagnetic effect. *J. Phys. Soc. Jpn* **88**, 024402 (2019).
45. Hehl, F. W., Obukhov, Y. N., Rivera, J.-P. & Schmid, H. Relativistic nature of a magnetoelectric modulus of $Cr_2 O_3$ crystals: a four-dimensional pseudoscalar and its measurement. *Phys. Rev. A* **77**, 022106 (2008).
46. Wang, J., Lei, C., MacDonald, A. H. & Binek, C. Dynamic axion field in the magnetoelectric antiferromagnet chromia Preprint at https://arxiv.org/abs/1901.08536 (2019).
47. Wang, H. et al. Dynamical axion state with hidden pseudospin Chern numbers in $MnBi_2 Te_4$-based heterostructures. *Phys. Rev. B* **101**, 081109(R) (2020).
48. Li, J. et al. Intrinsic magnetic topological insulators in van der Waals layered $MnBi_2 Te_4$-family materials. *Sci. Adv.* **5**, eaaw5685 (2019).
49. Otrokov, M. M. et al. Prediction and observation of an antiferromagnetic topological insulator. *Nature* **576**, 416 (2019).
50. Rienks, E. D. L. et al. Large magnetic gap at the Dirac point in Bi2Te3/$MnBi_2 Te_4$ heterostructures. *Nature* **576**, 423 (2019).
51. Deng, Y. et al. Quantum anomalous Hall effect in intrinsic magnetic topological insulator $MnBi_2 Te_4$. *Science* **367**, 895 (2020).
52. Chen, B. et al. Intrinsic magnetic topological insulator phases in the Sb doped $MnBi_2 Te_4$ bulks and thin flakes. *Nat. Commun.* **10**, 4469 (2019).
53. Klimovskikh, I. I. et al. Tunable 3D/2D magnetism in the $(MnBi_2 Te_4)(Bi_2 Te_3)_m$ topological insulators family. *npj Quantum Mater.* **5**, 54 (2020).
54. Yan, J.-Q. et al. Crystal growth and magnetic structure of $MnBi_2 Te_4$. *Phys. Rev. Mater.* **3**, 064202 (2019).
55. Hao, Y.-J. et al. Gapless surface dirac cone in antiferromagnetic topological insulator $MnBi_2 Te_4$. *Phys. Rev. X* **9**, 041038 (2019).
56. Chen, Y. J. et al. Topological electronic structure and its temperature evolution in antiferromagnetic topological insulator $MnBi_2 Te_4$. *Phys. Rev. X* **9**, 041040 (2019).
57. Zeugner, A. et al. Chemical aspects of the candidate antiferromagnetic topological insulator $MnBi_2 Te_4$. *Chem. Mater.* **31**, 2795 (2019).
58. Wu, J. et al. Natural van der Waals heterostructural single crystals with both magnetic and topological properties. *Sci. Adv.* **5**, eaax9989 (2019).
59. Vidal, R. C. et al. Topological electronic structure and intrinsic magnetization in $MnBi_4 Te_7$: A $Bi_2 Te_3$ derivative with a periodic Mn sublattice. *Phys. Rev. X* **9**, 041065 (2019).
60. Hu, C. et al. A van der Waals antiferromagnetic topological insulator with weak interlayer magnetic coupling. *Nat. Commun.* **11**, 97 (2020).
61. He, K. $MnBi_2 Te_4$-family intrinsic magnetic topological materials. *npj Quantum Mater* **5**, 90 (2020).
62. Lei, C., Chen, S. & MacDonald, A. H. Magnetized topological insulator multilayers. *Proc. Natl. Acad. Sci.* **117**, 27224 (2020).
63. Zhang, H. et al. Topological insulators in $Bi_2 Se_3$, $Bi_2 Te_3$ and $Sb_2 Te_3$ with a single Dirac cone on the surface. *Nat. Phys.* **5**, 438 (2009).
64. Liu, Z. & Wang, J. Anisotropic topological magnetoelectric effect in axion insulators. *Phys. Rev. B* **101**, 205130 (2020).
65. Liu, C.-X. et al. Oscillatory crossover from two-dimensional to three-dimensional topological insulators. *Phys. Rev. B* **81**, 041307 (2010).
66. Marsh, D. J. E., Fong, K. C., Lentz, E. W., Šmejkal, L. & Ali, M. N. Proposal to detect dark matter using axionic topological antiferromagnets. *Phys. Rev. Lett.* **123**, 121601 (2019).
67. Kresse, G. & Furthmüller, J. Efficient iterative schemes for ab initio total-energy calculations using a plane-wave basis set. *Phys. Rev. B* **54**, 11169 (1996).
68. García, A. & Cohen, M. L. First-principles ionicity scales. I. Charge asymmetry in the solid state. *Phys. Rev. B* **47**, 4215 (1993).
69. Perdew, J. P., Burke, K. & Ernzerhof, M. Generalized gradient approximation made simple. *Phys. Rev. Lett.* **77**, 3865 (1996).
70. Blöchl, P. E. Projector augmented-wave method. *Phys. Rev. B* **50**, 17953 (1994).
71. Marzari, N. & Vanderbilt, D. Maximally localized generalized Wannier functions for composite energy bands. *Phys. Rev. B* **56**, 12847 (1997).
72. Souza, I., Marzari, N. & Vanderbilt, D. Maximally localized Wannier functions for entangled energy bands. *Phys. Rev. B* **65**, 035109 (2001).
73. Pizzi, G. et al. Wannier90 as a community code: new features and application. *J. Phys.: Condens. Matter* **32**, 165902 (2020).

ACKNOWLEDGEMENTS

H.Z. acknowledge Jing Wang for helpful discussions. This work is supported by the Fundamental Research Funds for the Central Universities (Grant No. 020414380185), Natural Science Foundation of Jiangsu Province (No. BK20200007), the Natural Science Foundation of China (Grants No. 12074181 and No. 11834006) and the Fok Ying-Tong Education Foundation of China (Grant No. 161006).

AUTHOR CONTRIBUTIONS

H.Z. conceived the project. T.Z. and H.W. performed the derivations and calculations. H.Z., T.Z., H.W., and D.X. performed the data analysis. T.Z., H.W., and H.Z. wrote the manuscript with inputs from all the authors.

COMPETING INTERESTS

The authors declare no competing interests.

ADDITIONAL INFORMATION

Correspondence and requests for materials should be addressed to H.Z.

Reprints and permission information is available at http://www.nature.com/reprints

Publisher's note Springer Nature remains neutral with regard to jurisdictional claims in published maps and institutional affiliations.